Reappraisal of meridional differences of factors controlling phytoplankton biomass and of mechanisms that initiate the spring bloom in the northwestern Pacific Ocean

Eko Siswanto[*], Tetsuichi Fujiki, Kazuhiko Matsumoto, Makio C. Honda, Kosei Sasaoka, Toshiro Saino

Research Institute for Global Change (RIGC), Japan Agency for Marine-Earth Science and Technology (JAMSTEC), 2-15 Natsushima-cho, Yokosuka-city, Kanagawa 237-0061, Japan

*Corresponding author. Tel.: +81-46-867-9822

E-mail addresses: ekosiswanto@jamstec.go.jp (E. Siswanto); tfujiki@jamstec.go.jp (T. Fujiki); matsumotok@jamstec.go.jp (K. Matsumoto); hondam@jamstec.go.jp (M. Honda); sasaoka@jamstec.go.jp (K. Sasaoka); tsaino@jamstec.go.jp (T. Saino)

ABSTRACT

Multiplatform observations of ocean biogeochemical data were used to elucidate meridional differences in the factors that limit phytoplankton biomass (*Chl-a*) and the mechanisms that trigger the spring phytoplankton bloom in the northwestern Pacific Ocean (NWPO). During the winter, *Chl-a* north (south) of 30°N is limited by light (nutrients). During the spring and fall, *Chl-a* in much of the area east of the Japan/Kuril Islands and/or north of 40°N (south of 35°N) is limited by light (nutrients). During the summer, nutrients limit *Chl-a* over much of the NWPO, except in the areas east of the Japan/Kuril Islands and north of 45ºN. In the area south of around 30ºN phytoplankton biomass is nutrient limited throughout the year, and the onset of the spring bloom is likely hidden by rapid phytoplankton growth, which begins in the fall and is associated with mixed layer deepening. Between 30ºN and 40ºN, the bloom onset is mainly associated with a cessation of mixed layer deepening. In much of the area north of 40ºN, including the Oyashio area, the onset of the spring bloom is consistent with Sverdrup's critical depth hypothesis. The spatial extents of the light- and nutrient-limited areas and the areas associated with a single bloom onset mechanism are by no means constant. They are expected to undergo meridional shifts as a result of large-scale climatic changes and global warming.

1. Introduction

The northwestern Pacific Ocean (NWPO) comprises the western part of two main gyres, the cyclonic North Pacific Subarctic Gyre and the anticyclonic North Pacific Subtropical Gyre. The subarctic gyre is bordered by the Oyashio cold current in the west and is a well-known high-nutrient and low-chlorophyll area, whereas the subtropical gyre is bordered by the Kuroshio warm current in the west and is characterized by low nutrient concentrations. The Kuroshio and Oyashio currents meet and interact east of Japan in the Kuroshio-Oyashio confluence area (Fig. 1a), which separates the subtropical anticyclonic gyre from the subarctic cyclonic gyre (e.g., Hanawa and Mitsudera, 1987; Yasuda, 2003).

Previous studies have shown that phytoplankton biomass (chlorophyll-*a* concentration, hereafter *Chl-a*, mg m^{-3}) is light-limited in the subarctic area (SAA) but nutrient-limited in the subtropical area (STA) (e.g., Limsakul et al., 2002; Fujiki et al., 2014). However, the areas within which *Chl-a* is light-limited in the SAA and nutrient-limited in the STA may change seasonally, and these changes have not been detailed previously.

An empirical way to determine the spatial extent of light or nutrient limitation, as well as to identify the probable underlying processes, is to assess the associations between *Chl-a* and environmental variables. The ability to discern these relationships on a seasonal basis has the potential to provide valuable understanding of the footprints of large-scale climate changes such

3

55   as global warming on biogeochemical variability in the NWPO and its probable driver(s) in

56   different seasons. The reason is that large-scale climate variability, such as long-term geophysical

57   trends and the El Niño/Southern Oscillation and Pacific Decadal Oscillation, seem to have

58   seasonally dependent impacts on NWPO *Chl-a* variability (e.g., Freeland et al., 1997; Whitney

59   and Freeland, 1999; Chiba et al., 2004; Goes et al., 2004; Wang et al., 2008).

60   Geophysical variables also determine the onset of the phytoplankton spring bloom, a well-

61   known phenomenon, in both the SAA and the STA (e.g., Limsakul et al., 2002; Yoo et al., 2008;

62   Fujiki et al., 2014). For more than half a century, Sverdrup's critical depth (*CD*, m) hypothesis

63   (e.g., Siegel et al., 2002; Obata and Ishizaka, 1996) has served biological oceanographers as the

64   basic tenet of the mechanism underlying initiation of the spring phytoplankton bloom. The *CD*

65   hypothesis envisions that the spring bloom starts when the mixed layer depth (*MLD*, m) becomes

66   shallower than the *CD* (Sverdrup, 1953), and the nutrient is not limiting factor as a prerequisite.

67   By definition, the *CD* is the depth above which the vertically integrated net phytoplankton

68   production equals the vertically integrated loss (Sverdrup, 1953).

69   Results of recent studies in different oceans have mentioned that the onset of the spring

70   phytoplankton bloom is not always consistent with the *CD* hypothesis. Using ocean color sensor-

71   retrieved *Chl-a* data, Behrenfeld (2010) has proposed an alternative 'dilution-recoupling'

72   hypothesis that attributes the onset of the North Atlantic Ocean spring bloom to decoupling of the

73 specific growth rates and loss rates of the phytoplankton while the mixed layer is deepening, the

74 assumption being that the phytoplankton are well mixed and that nutrient concentrations are not

75 limiting to their growth during that time. On the basis of satellite-derived *Chl-a* data from the east

76 coast of New Zealand, Chiswell (2011) has proposed a 'stratification-onset' hypothesis that

77 attributes the initiation of the spring bloom to a cessation of deep vertical mixing, which allows

78 *Chl-a* to increase in the near-surface, actively mixed layer. Similar to Chiswell's (2011) hypothesis,

79 Taylor and Ferrari (2011) and Shiozaki et al. (2014) have argued that the phytoplankton spring

80 bloom in the North Atlantic Ocean and the region south of the Kuroshio extension in the NWPO,

81 respectively, may also be initiated by a 'turbulence weakening' or 'turbulence shutdown' that

82 increases the residence time of the phytoplankton in the euphotic layer, without a prerequisite of

83 *MLD* shoaling.

84   Although Obata and Ishizaka (1996) have mentioned that the *CD* hypothesis can in general

85 explain the initiation of the spring bloom in the NWPO, Shiozaki et al. (2014) have shown that the

86 *CD* mechanism applies mainly in the waters of the Oyashio Current and in the region north of the

87 Kuroshio extension in the NWPO. Shiozaki et al. (2014) have shown that there are regional

88 differences in the mechanisms responsible for the onset of the spring bloom in the NWPO, but the

89 detailed spatial features of the mechanism responsible for the onset of the spring bloom have not

90 yet been fully delineated, because their analysis was based on regional averages and was

5

91   meridionally constrained within the region from 30°N to 45°N.

92   Here, using ocean color data from both the Sea-viewing Wide Field-of-Sensor (SeaWiFS)

93   and the Moderate Resolution Imaging Spectroradiometer-Aqua (MODIS), we have revisited the

94   NWPO (140–165°E, 27–53°N), including both the SAA and the STA, within which

95   biogeochemical time-series stations K2 (160°E, 47°N) and S1 (145°E, 30°N), respectively, are

96   located (Fig. 1a). By also analyzing other sensor-retrieved and reanalyzed oceanographic and

97   atmospheric geophysical variables at the scale of pixels, our aim was to gain an understanding of

98   meridional differences in (1) the associations between *Chl-a* and geophysical variables that could

99   be used as proxies to assess the factors that limit and control *Chl-a* variations in different seasons,

100   and (2) the mechanisms that initiate the spring phytoplankton bloom in the NWPO. Our strategy

101   was to apply this understanding to analysis of data collected from the K2 (representing the SAA)

102   and S1 (representing the STA) biogeochemical time series stations, where ship-borne observations

103   were made from the research vessel *Mirai* multiple times each year from 2010 to 2012. Satellite

104   and reanalyzed data derived at stations K2 and S1 were verified using in situ data collected at the

105   same stations.

106

107

2. Methodology

2.1. Multi-platform data acquisitions

We used monthly SeaWiFS and MODIS-retrieved *Chl-a*, diffuse attenuation coefficients at

490 nm (Kd_{490}, m^{-1}), and photosynthetically available radiation (*PAR*, mol photons m^{-2} d^{-1}, 400–

700 nm radiation) retrieved from September 1997 to June 2013 (http://oceancolor.gsfc.nasa.gov).

The spatial resolution of the data was 9 km. We used monthly *SST*s retrieved by the Advanced

Very High Resolution Radiometer (AVHRR, http://podaac.jpl.nasa.gov/AVHRR-Pathfinder) and

MODIS (http://oceancolor.gsfc. nasa.gov) during the same period.

To provide concurrent monthly *MLD* data, we acquired reanalyzed *MLD*s from the Global

Ocean Data Assimilation System (GODAS, https://climate dataguide.ucar.edu) with 1° spatial

resolution and Argo float-based *MLD*s from the Japan Agency for Marine Earth Science

(JAMSTEC, http://www.jamstec.go.jp/ARGO/argo_web/argo/index. html). We also used monthly

Cross-Calibrated Multi-Platform (CCMP) and monthly WindSat-derived wind speed (*WS*, m s^{-1})

data, both of which had 0.25° spatial resolution and were acquired from

http://apdrc.soest.hawaii.edu.

2.2. Filling missing data and converting two datasets from different sensors/platforms

We applied a Data Interpolating Empirical Orthogonal Function (DINEOF) method (Alvera-

7

125   Azcarate et al., 2007) separately to the SeaWiFS, MODIS, AVHRR, and Argo float-derived data

126   to construct spatially complete SeaWiFS (*Chl-a*), MODIS (*Chl-a*, *SST*), AVHRR (*SST*), and Argo

127   float (*MLD*) datasets. Details of the procedures for implementing DINEOF can be found at

128   http://modb.oce.ulg.ac.be/mediawiki/index.php/DINEOF. We filled in missing data to ensure that

129   the statistics derived from the analysis of our results, mainly correlation coefficients between *Chl-*

130   *a* and geophysical variables and their levels of significance, could be compared pixel by pixel,

131   because the statistics for all the pixels were associated with the same number of degrees of freedom.

132   To ensure compatibility of the *Chl-a* and *PAR* data retrieved by SeaWiFS and MODIS, pixel-

133   based linear regressions were applied during the period from July 2002 to December 2010, when

134   the observations of both sensors overlapped. Regression coefficients for each pixel were then used

135   to transform all MODIS data so that they were compatible to SeaWiFS data. Finally, we used

136   SeaWiFS data from September 1997 to December 2007 and the transformed MODIS data from

137   January 2008 to June 2013 for further spatiotemporal analysis. We refrained from using post-2008

138   SeaWiFS data because there were some problems and/or missing data during some periods before

139   the end of the mission. We transformed *Chl-a* data from MODIS to SeaWiFS (rather than the

140   reverse transformation from SeaWiFS to MODIS) because the uncertainty of the SeaWiFS *Chl-a*

141   data in the NWPO has been confirmed to be less than $\pm35\%$ (see Sasaoka et al., 2002), which is

142   the goal for the uncertainty of the NASA ocean color mission *Chl-a* product (O'Reilly et al., 1998).

8

143   Within the period of overlapping AVHRR and MODIS observations (July 2002 to December 2009),

144   we derived pixel-by-pixel regression coefficients of AVHRR *SST*s on MODIS *SST*s and used them

145   to transform MODIS *SST*s so that they were compatible with AVHRR *SST*s. We then used AVHRR

146   *SST*s from September 1997 to December 2009 and transformed MODIS *SST*s from January 2010

147   to June 2013 in the subsequent analysis.

148   We transformed GODAS *MLD*s so that they were compatible with Argo float-based *MLD*s,

149   which are defined as the depths at which the density differs from the density at the sea surface

150   ($\Delta\sigma_\theta$) by 0.125 kg m^{-3} (Monteley and Levitus, 1997). Pixel-by-pixel regression coefficients were

151   derived by using *MLD* datasets collected from January 2007 (because of the large Argo *MLD*

152   dataset available since January 2007) to June 2013. We then used transformed GODAS *MLD*s

153   from June 1997 to December 2006 and Argo *MLD*s from January 2007 to June 2013 in subsequent

154   spatiotemporal analysis. We did not apply DINEOF to GODAS *MLD* and *WS* data because there

155   were no spatial gaps in the data, but we transformed Windsat *WS* data so that they were compatible

156   with CCMP *WS* data by using regression coefficients derived during the time interval when their

157   observations overlapped (February 2003 to December 2012).

158   Variations of the correlation coefficients along the K2–S1 meridional section between pairs

159   of variables measured by different sensors/platforms are shown in Fig. 1b. The fact that all of the

160   correlation coefficients (>0.5) were statistically significant at $p < 0.05$ indicated that data retrieved

161   by the different sensors/platforms, when appropriately transformed, could be used for analysis of

162   spatiotemporal variations. We followed Cohen et al. (2009) by defining boreal seasons as follows:

163   winter, January–March; spring, April–June; summer, July–September; and fall, October–

164   December.

165   Fig. 1 (around here)

166   *2.3. Estimations of sea surface nitrate, phytoplankton growth rate, and critical depth*

167   To characterize nutrient variability, we estimated surface nitrate concentrations (*SSN*s, µM)

168   by applying the empirical *SSN* model of Goes et al. (2000) as follows:

169    $SSN = 25.22 - 1.96\,(SST) + 0.04\,(SST)^2 - 1.21\,(Chl\text{-}a) - 0.05(Chl\text{-}a)^2$ (1)

170   Eq. (1) was derived by Goes et al. (2000) by using in situ data collected in the North Pacific Ocean

171   exclusive of the equatorial region.

172   To capture the onset of the spring bloom, we calculated the percentage increase of *Chl-a* per

173   month as a proxy of phytoplankton growth rate (*r*, % per month) using the following equation:

174    $r = 100 \left(\dfrac{(Chl\text{-}a1 - Chl\text{-}a0)}{Chl\text{-}a0} \right)$ (2)

175   where *Chl-a*0 and *Chl-a*1 are the initial *Chl-a* and the *Chl-a* after a time interval of one month,

176   respectively. Generally, we considered the rapid increase of *Chl-a* after the period of lowest winter

10

177　*Chl-a* (e.g., Taylor and Ferrari, 2011; Shiozaki et al., 2014) as the onset of the spring bloom.

178　　　We approximated the *CD* by using a simplified form of Sverdrup's (1953) *CD* equation noted

179　by Parsons et al. (1984) as follows:

180　$$CD = \frac{0.5\ PAR}{Kd_{PAR}\ I_c} \tag{3}$$

181　where Kd_{PAR} (m^{-1}) and I_c (mol photons m^{-2} d^{-1}) are the attenuation coefficient of *PAR* and *PAR* at

182　the compensation depth, respectively. The factor of 0.5 was used to reduce *PAR* due to absorption

183　of the longer and shorter wavelengths of light in the first few cm of the water column (Parsons et

184　al., 1984; Okamoto et al., 2010). We used a constant I_c of 1.14 mol photons m^{-2} d^{-1} (Parsons et al.,

185　1984; Okamoto et al., 2010; Shiozaki et al., 2014) and Eq. (4) below:

186　$$Kd_{PAR} = 0.0665 + 0.874\ Kd_{490} - \frac{0.00121}{Kd_{490}} \tag{4}$$

187　to obtain Kd_{PAR} from Kd_{490} data (Morel et al., 2007).

188　*2.4. Ship-borne observations*

189　　　Ship-borne observations were conducted onboard the research vessel *Mirai* from 2010 to

190　2012 at biogeochemical time-series stations K2 and S1 (Fig. 1a, Table 1). In situ values of *Chl-a*,

191　*SSN*, *MLD*, *PAR*, and *CD* (estimated from in situ surface and underwater *PAR*s) at those stations

192　were used to verify satellite and reanalyzed data.

193   Table 1. (around here)

194   Surface water samples for in situ surface *Chl-a* measurements were directly transferred from

195   a bucket into polyethylene bottles and immediately filtered through 25-mm glass fiber filters

196   (Whatman GF/F). The fluorescence of the particulate matter collected on the filters was then

197   measured on board with a Turner Design Fluorometer (10-AU, Turner Design, Inc.) following the

198   methodology of Holm-Hansen and Riemann (1978) after extraction in *N,N*-dimethylformamide.

199   Surface water samples were also collected for *SSN* analysis. *SSN* was measured on board with a

200   QuAAtro 2-HR AutoAnalyzer (BLTEC K. K., Osaka, Japan).

201   Vertical profiles of density derived from data collected with a SBE 9/11 plus conductivity-

202   temperature-depth profiler (SeaBird Inc., Bellevue, WA, USA) were used to define the *MLD*. To

203   be consistent with Argo float-based *MLD*s, we used $\Delta\sigma_\theta = 0.125$ kg m^{-3} (Monteley and Levitus

204   (1997) to define the in situ *MLD*. The in situ *CD* used in this study was calculated by using Eq. (3)

205   with the values of the in situ surface *PAR* and underwater *PAR* (which was used to determine Kd_{PAR}),

206   which were recorded by a PUV-510B radiometer (Biospherical Instruments, Inc., San Diego, CA,

207   USA) and SeaWiFS profiling multichannel radiometer (Satlantic, Inc., Halifax, Nova Scotia,

208   Canada), respectively.

209

210 *2.5. Satellite and reanalyzed data verification method*

211   An ideal verification analysis would have involved satellite or calculated data collected

212 concurrently with in situ observations (e.g., Bailey and Werdell, 2006; Siswanto et al., 2011). We

213 were unable to carry out such an analysis because our in situ data (daily measurements) and the

214 satellite and calculated data (monthly composites) were available on different time scales, and

215 calibration/validation of the satellite data was beyond the scope of this study. Because our study

216 emphasized the seasonal timescale, we constructed monthly means of in situ data collected during

217 the same months (though in different years).

218   Verification of satellite and/or reanalyzed data was conducted by estimating systematic

219 errors (relative percentage differences) for the monthly means of in situ variables other than *Chl-*

220 *a* and the absolute errors (absolute percentage difference or uncertainty) for the monthly means of

221 in situ *Chl-a*. Relative and absolute percentage differences were computed by using equations in

222 Bailey and Werdell (2006) and Siswanto et al. (2011).

223 **3. Results**

224 *3.1. Verification of satellite-derived and reanalyzed data*

225   Although the satellite and in situ *PAR*s evidenced similar seasonality (Fig. 2a, 2h), satellite

226 *PAR*s overestimated in situ *PAR*s, the relative percentage differences being 42.8% and 31.2% at

227   stations K2 and S1, respectively (Table 2). The satellite *PAR* overestimations could be attributed

228   to the fact that in situ *PAR*s were based on daily measurements, which were very much affected by

229   clouds, whereas satellite *PAR*s were modeled using plane-parallel theory, which assumes that the

230   effects of clouds and other atmospheric constituents can be decoupled (e.g., Frouin and Pinker,

231   1995; Frouin and McPherson, 2012).

232   The seasonalities of satellite-based and in situ *CD*s were similar, but satellite *CD*s

233   overestimated in situ *CD*s by 25.7% and 15.3% at stations K2 and S1, respectively (Fig. 2i, 2p;

234   Table 2). Overestimation of satellite *CD*s can be attributed to overestimation of satellite *PAR* (Fig.

235   2a, 2h). The seasonal cycles of reanalyzed *MLD*s at stations K2 and S1 were in good agreement

236   with in situ *MLD*s (Fig. 2i, 2p). Overall, reanalyzed *MLD*s underestimated in situ *MLD*s by 4.3%

237   at station K2 but overestimated in situ *MLD*s by 15.2% at station S1.

238   Estimated *SSN*s at station K2 were in good agreement with in situ *SSN*s, the relative

239   percentage difference being –2.5% (Fig. 2a, Table 2). Estimated *SSN*s at station S1, however, very

240   much overestimated in situ *SSN*s, the relative percentage difference being >500% (Fig. 2h). The

241   fact that estimated *SSN*s were higher than in situ *SSN*s at station S1, which was characterized by

242   low in situ *SSN*s (<0.5 µM) throughout the year, indicates that the *SSN* algorithm produced biased

243   estimates in an area with low *SSN*s. Goes et al. (2000, their figure 1b) also show overestimates of

244   low in situ *SSN*s.

245   The seasonalities of satellite and in situ *Chl-a* at stations K2 and S1 were generally similar

246   (Fig. 2i, 2p). Although overestimates of satellite *Chl-a* were apparent, especially during late

247   spring/summer at station K2 and during winter/early spring at station S1, the absolute percentage

248   difference (uncertainty) of satellite *Chl-a* was overall less than the *Chl-a* retrieval uncertainty

249   targeted by NASA's ocean color mission (±35%, O'Reilly et al., 1998; Sasaoka et al., 2002). At

250   stations K2 and S1 the absolute percentage differences were 15.6% and 23.4%, respectively.

251   Table 2. (around here)

252   Because the satellite and reanalyzed data were in general associated with low systematic errors

253   (except for the calculated *SSN*s at station S1), and most importantly, because the uncertainty of the

254   *Chl-a* values met NASA's ocean color mission goal, we concluded that satellite and reanalyzed

255   data could be used to capture the seasonal cycles of the in situ data. Based on the assumption that

256   the errors in the estimates derived from satellite and reanalyzed data at stations K2 and the S1

257   could be extrapolated to the entire NWPO, we concluded that our satellite and reanalyzed data

258   were suitable for subsequent spatiotemporal analysis. We anticipated that the estimated *SSN*s for

259   the SAA and STA would tend to be higher than the in situ *SSN*s, but we expected the seasonal

260   patterns to be similar. The association between *Chl-a* and *SSN* was therefore not much affected by

261   *SSN* overestimation, because the seasonal pattern (rather than the magnitude of the values) was

262   more important in determining the association between the two variables.

15

263   *3.2. Meridional and seasonal associations between chlorophyll-a and geophysical variables*

264   Fig. 2 shows the seasonal cycles of *Chl-a* and geophysical variables at several latitudes along

265   the K2-to-S1 line. Except for the *SSN*s in the lower latitudes, all variables showed distinct seasonal

266   cycles. Unlike the seasonal cycles of the geophysical variables, which were similar at all latitudes

267   along the K2-S1 section, there were conspicuous meridional differences of the *Chl-a* seasonal

268   cycles in terms of both the amplitudes and patterns of the cycles (Fig. 2i–p). Consistent with the

269   patterns detailed by Yoo et al. (2008), the *Chl-a* concentrations were higher throughout the year in

270   the SAA than in the STA, and the *Chl-a* spring bloom took place progressively earlier from south

271   to north. It is apparent that the *Chl-a* peaks during the spring at latitudes of 30°N (S1), 35°N, 40°N,

272   and both 45°N and 47°N (K2) were observed around March, April, May, and June, respectively.

273   The fact that the seasonal cycle of *Chl-a* was less obvious at 42.5°N may reflect a transition of the

274   *Chl-a* seasonal cycle from the SAA seasonal cycle (with a winter minimum) to the STA seasonal

275   cycle (with a summer minimum).

276   It is well known that the observed seasonal cycle of *Chl-a* (Fig. 2i–p) is the most dominant

277   mode of overall *Chl-a* variability in the NWPO (e.g., Yoder and Kennelly, 2003; Vantrepotte and

278   Me´lin, 2009; Thomas et al., 2012). When all monthly data (all seasons) were included in the

279   analysis (degrees of freedom = 188, N = 190), at $p < 0.05$ *Chl-a* was positively (negatively)

280   correlated to *WS*, *MLD*, and *SSN* (Fig. 3a–c) in the south (north) area, but negatively (positively)

16

281   correlated with *SST* and *PAR* (Fig. 3d–e) in the south (north) area. The areas (with no significant

282   correlation, see white areas along 40°N) between those two contrasting areas were transitional

283   areas where there was no apparent *Chl-a* seasonal cycle (Fig. 2k).

284   Fig. 2. (around here)

285   Fig. 3. (around here)

286   The positive correlations between *Chl-a* and *MLD* (or *WS*), and between *Chl-a* and *SSN* in

287   the STA south of about 40°N (Fig. 3a–c) may be an indication of nutrient limitation of

288   phytoplankton biomass. In contrast, in the SAA north of 40°N, the negative correlation between

289   *Chl-a* and *MLD* (or *WS*) and the positive correlation between *Chl-a* and *PAR* may indicate light

290   limitation of phytoplankton biomass. However, when the datasets spanned annual cycles,

291   significant correlations between *Chl-a* and geophysical variables were obscured by the close

292   coupling of the seasonal cycles of the datasets. For instance, there were similar (inverse) seasonal

293   cycles between *Chl-a* and *MLD*, *WS*, and *SSN* in the STA (the SAA).

294   Correlations during individual seasons would to some degree be unaffected by correlations

295   associated with the similarities or dissimilarities of seasonal cycles, as variability in other seasons

296   would not be taken into account. These correlations would thus be more indicative of intraseasonal

297   associations between *Chl-a* and geophysical variables. To discern the associations between *Chl-a*

298   and geophysical variables in the absence of artifacts associated with seasonal cycles, we filtered

299   out the seasonal cycles and detrended the data. The resultant associations between *Chl-a* and

300   geophysical variable anomalies are also presented in the following sections.

301   3.2.1. Winter chlorophyll-*a* and geophysical variable associations

302   The patterns of increasing *Chl-a* (Fig. 2i–p), increasing *PAR*, and decreasing *WS* (Fig. 2a–h)

303   during the winter led to significant ($p < 0.05$), positive correlations between *Chl-a* and *PAR*, and

304   to negative correlations between *Chl-a* and *WS* over a wide east–west, belt-like area extending

305   meridionally from about 30°N to 40°N (Fig. 4e, 4m). Nutrients were not limiting to phytoplankton

306   biomass, because the *MLD* was increasing and eventually exceeded the *CD* (Fig. 2i–p, 6a–c).

307   Vertical mixing was therefore able to transport phytoplankton to the light-limited region of the

308   water column. The positive correlation between *Chl-a* and *PAR* might therefore be an indication

309   of light limitation of phytoplankton biomass. The remarkable positive correlations between *Chl-a*

310   and *MLD* and between *Chl-a* and *SSN* primarily in the area south of 30°N, in contrast, might

311   indicate that phytoplankton biomass was nutrient limited in that area. The fact that the *MLD* was

312   less than the *CD* south of 30°N (Fig. 6a–c, see also Obata and Ishizaka, 1996) suggests that light

313   was no longer limiting to phytoplankton biomass.

314   Analysis of variable anomalies (after removal of seasonal means and trends) revealed that in

315   the area north of 30°N there were still significant positive correlations between *Chl-a* and *PAR*

316 (Fig. 5e). The fact that the same area was characterized by negative correlations between *Chl-a*

317 and *WS* (hence *MLD*) (Fig. 5m, 5q) confirms that *Chl-a* variations in the area north of 30°N were

318 indeed limited by light during the winter. In the area south of 30°N, there were still positive

319 correlations between *Chl-a* and *MLD*, and between *Chl-a* and *SSN* (Fig. 5i, 5q). These correlations

320 confirmed that on both intraseasonal and non-seasonal timescales, phytoplankton biomass south

321 of 30°N was nutrient-limited during the winter. The transitional area separating light-limited from

322 nutrient-limited areas thereby shifted to around 30°N. An elongated band extending from 145°E,

323 35°N southeastward was characterized by a negative correlation between *Chl-a* and *SST* and a

324 positive correlation between *Chl-a* and *SSN* (but unaccompanied by a clear, elongated pattern of

325 correlation between *Chl-a* and *MLD*), the indication being that physical processes other than

326 conventional vertical mixing might underlie the *Chl-a* variations.

327 Fig. 4 (around here)

328 Fig. 5 (around here)

329 3.2.2. Spring chlorophyll-*a* and geophysical variable associations

330 During the spring, light and temperature were presumably not limiting factors, because *PAR*

331 and *SST* were already high (Fig. 2a–h), and the *MLD* was already less than the *CD* (Fig. 2i–p, 6d–

332 f). Therefore, the negative correlations between *Chl-a* and *SST* and *PAR* (Fig. 4b, 4f) in the area

19

333   south of 40°N were mainly a reflection of the close coupling of their seasonality (Fig. 2e–h, 2m–

334   p), because these negative correlations are inconsistent with basic understanding of the

335   physiological effects of light and temperature on phytoplankton growth (Eppley, 1972; Behrenfeld

336   and Falkowski, 1997). The positive correlations between *Chl-a* and *MLD*, accompanied by positive

337   correlations between *Chl-a* and *SSN* (Fig. 4j, 4r) in the same southern area, were also a

338   manifestation of the close coupling of their seasonalities (i.e., concurrent seasonal decreases of

339   *Chl-a*, *MLD*, and *SSN*). Accompanying these synchronized seasonal changes, however, there may

340   be ecological processes such as increases of grazing pressure, decreases of nutrient concentrations

341   due to consumption by phytoplankton, and weakening of vertical mixing. Phenomena that

342   contrasted to what was observed in the area south of 40°N were observed in the area north of about

343   45°N.

344   Analysis of variable anomaly correlations revealed that the area within which variations of

345   phytoplankton biomass reflected nutrient availability was primarily confined to the area south of

346   about 32.5°N, as evidenced by the positive correlations between *Chl-a* and *MLD* and *SSN* (Fig. 5j,

347   5r) and the negative correlation between *Chl-a* and *SST* (Fig. 5b) in that region. Light limitation

348   of phytoplankton biomass was primarily confined to the area west of the K2-S1 section (east of

349   the Japan/Kuril Islands) and/or north of 40°N, as evidenced by the negative correlation between

350   *Chl-a* and *MLD* and the positive correlation between *Chl-a* and *PAR* in that region.

351   3.2.3. Summer chlorophyll-*a* and geophysical variable associations

352   During the summer the *MLD* was shallower, the *CD* deeper, and the *SST* higher than during

353   any other season, and the *PAR* was high (Fig. 2a–h, 2i–p). The implication is that phytoplankton

354   biomass was not limited by light or temperature during the summer. The positive correlations

355   between *Chl-a* and *MLD* and *WS* (Fig. 4o, 4s) apparent over the area east and west of the K2–S1

356   section might thus indicate nutrient limitation of phytoplankton biomass, because the very shallow

357   summer *MLD* (strongest stratification) limits nutrient fluxes from within the nutricline into the

358   mixed layer. This apparently nutrient-limited condition was especially apparent in the area south

359   of about 42.5ºN, as indicated by the negative correlations between *Chl-a* and *SST* in that region

360   (Fig. 4c).

361   Analysis of variable anomalies indicated that *Chl-a* variations in much of the NWPO were

362   indeed primarily controlled by nutrient supplies, especially along and west of the K2–S1 section.

363   The observed positive correlations between *Chl-a* and *MLD* and *WS*, and the negative correlations

364   between *Chl-a* and *SST* (Fig. 5c, 5o, 5s) are consistent with this scenario. The negative correlations

365   between *Chl-a* and *SSN* south of 35ºN (Fig. 4k, 5k) and between *Chl-a* and *MLD* south of 30ºN

366   (Fig. 4s, 5s) were, however, inconsistent with nutrient limitation.

367

368   3.2.4. Fall chlorophyll-*a* and geophysical variable associations

369   Fall was a season when the NWPO was divided almost symmetrically into two contrasting

370   areas. The area south of 40ºN seemed to be nutrient limited, and the area north of 40ºN was

371   apparently light limited (Fig. 4d, 4h, 4l, 4p, 4t). During the fall there was a departure from the

372   lowest nutrient concentrations characteristic of the summer. The *Chl-a* and *SSN* concentrations

373   increased, the *MLD* deepened, and there were strong associations between *Chl-a* and *MLD* and

374   *SSN* and in the area south of 40ºN (Fig. 2e-h, 2m-p). These observations indicate that ecological

375   processes (rather than just seasonality similarities) were responsible for the variability of *Chl-a*

376   during the fall. There was an increase in the supply of nutrients driven by a deepening of the *MLD*

377   that resulted in an increase of the *Chl-a*. The implication is that phytoplankton biomass south of

378   40ºN was more responsive to and thereby limited by nutrients during the fall. Further deepening

379   of the mixed layer in the area south of 40ºN would have entrained additional nutrients. Both *PAR*

380   and *SST* were high enough to maintain phytoplankton growth until the *MLD* exceeded the *CD*, and

381   besides entraining nutrients, deepening of the *MLD* probably led to dilution effects that decoupled

382   phytoplankton growth and losses (e.g., Yoshie et al., 2003; Behrenfeld, 2010).

383   The phytoplankton biomass north of 40ºN was likely more responsive to light for several

384   reasons. Macronutrient concentrations in this area were depleted to a level that would cause only

385   marginal limitation of phytoplankton growth (see Fujiki et al., 2014), and deepening of the *MLD*

386 (deeper than the *CD*) was accompanied by reductions of *PAR* and *SST* to levels lower than those

387 south of 40ºN. Increases of the *MLD* seemed to be more effective in causing light limitation than

388 in reducing grazing pressure via dilution effects that decouple phytoplankton growth and losses.

389   Analysis of variable anomalies indicated that the areas of light and nutrient limitation were

390 similar in the fall and spring. Nutrient limitation of phytoplankton biomass was apparent mainly

391 in the area south of 35ºN (Fig. 5t); light limitation was less widespread in the area west of the K2-

392 S1 line (east of the Japan/Kuril Islands) and/or north of 40ºN (Fig. 5h, 5p, 5t). Relationships

393 between *Chl-a* and *SSN* seemingly inconsistent with the nutrient limitation hypothesis were

394 apparent during the fall in the area south of 30ºN (Fig. 4l) and south of 35ºN (Fig. 5l).

395 *3.3. Meridional differences of the mechanism responsible for the onset of the phytoplankton spring*

396 *bloom*

397   At station S1 (Fig. 2p) and throughout much of the area south of 31ºN (Fig. 8a), a winter

398 (February/March) bloom was apparent. However, a remarkable, rapid increase of *Chl-a* was

399 already apparent during the fall when the *MLD* was deepening. The *Chl-a* also steadily increased

400 during the fall, and the expected decline of *Chl-a* due to light-limited conditions during the winter

401 did not occur. The fact that there was little or no light limitation during winter was evidenced by

402 the fact that the *MLD* was relatively shallow, roughly the same as the *CD* (Fig. 2p, 6a–c).

23

403   The area that was characterized by a remarkable *Chl-a* increase during the fall, by a steady

404   increase of *Chl-a* during the winter (Fig. 7k–l, 7a–c), and by a relatively shallow winter *MLD* (Fig.

405   6a–c) was largely confined to the area south of about 31°N. In that area, it was clear that the *Chl-*

406   *a* was already decreasing when the *MLD* was shoaling and had become much shallower than the

407   *CD*. These observations are clearly inconsistent with the hypothesis that shoaling of the *MLD*

408   above the *CD* is the mechanism that initiates the spring bloom. The rationale behind the *CD*

409   paradigm is that the spring bloom is initiated when the late winter *MLD* shoals above the *CD* at a

410   time when nutrients are not limiting to phytoplankton growth.

411   Spring blooms in the area from 32.5°N to 40°N were more pronounced and took place later,

412   in April or May (Fig. 2l–o, Fig. 8a), than in the areas south of 32.5°N. From west to east within

413   this latitude band, a decline of *Chl-a* (negative growth) during late fall and/or winter was clearly

414   apparent (Fig. 2l–o, 7a, 7l). This negative growth was a manifestation of severe light-limited

415   conditions, because the *MLD* was much deeper than the *CD* (Fig. 2l–o, 6a, 6l). Rapid and

416   remarkable increases of *Chl-a* were observed around March and/or April (Fig. 7c-d). Note that we

417   associated remarkable and rapid increases of *Chl-a* to increases of *Chl-a* that reached 20% per

418   month. Such rates of increase seemed to be characteristic of the onset of the spring bloom.

419   The initiation of the spring bloom (March/April) within the latitude band from 32.5°N to

420   40°N coincided with the cessation of winter mixed layer deepening (Fig. 2i–o), and when the *MLD*

421   had become much shallower than the *CD* (around May), the *Chl-a* concentrations were already

422   decreasing (negative growth, Fig. 7e–f). These results are inconsistent with the *CD* hypothesis as

423   the explanation for the onset of the spring bloom, although nutrient concentrations were not a

424   limiting factor during the winter. The onset of the bloom occurred only after the cessation of mixed

425   layer deepening and at a time when the *MLD* (although shoaling) was still much deeper than the

426   *CD*. This scenario is consistent with the 'stratification-onset' hypothesis proposed by Chiswell

427   (2011) and with the paradigm of Taylor and Ferrari (2011) and Shiozaki et al. (2014), who

428   associated the onset of the spring bloom with a 'turbulence weakening/shutdown'.

429   Figure 6. (around here)

430   Figure 7. (around here)

431   From roughly 42.5°N northward, where the K2 station was located, the spring bloom peaked

432   in late spring and was preceded by consistently low *Chl-a* concentrations during the winter (Fig.

433   2i–k, 8a). From fall (November) to at least January, the negative growth rates that were observed

434   (Fig. 2i–k, 7a, 7k–l) can likely be attributed to light limitation, because the *MLD* was remarkably

435   deeper than the *CD* (Fig. 6a, 6k-l). A rapid and remarkable increase of *Chl-a* (Fig. 2i–k, 7e–f) was

436   apparent only while the *MLD* was shoaling and was much shallower than the *CD* (Fig. 2i–k, 6d).

437   The onset of the spring bloom north of 42.5°N (including station K2) was therefore largely

438   consistent with Sverdrup's (1953) classic *CD* hypothesis. The relevance of the *CD* hypothesis in

439　this region reflects the fact that nutrient concentrations, because of the maximum winter

440　entrainment, were not limiting, and light limitation during the winter was more severe (due to

441　lower *PAR*) than in areas further to the south.

442　　　　　　　　　　　　　　　　Figure 8. (around here)

443　　　　　　　　　　　　　　　　Figure 9. (around here)

444　　　　　Compared to other northern areas (north of 42.5°N), the shoaling of the *MLD* until it became

445　shallower than the *CD* occurred earlier in the Oyashio area (March, Fig. 6c). However, the rapid

446　and remarkable increase of *Chl-a* in the Oyashio area also occurred earlier in April (Fig. 7d) than

447　in the other northern areas. Therefore, although the onset of the bloom took place earlier in the

448　Oyashio area than in most of the other areas to the north of 42.5°N, the onset of the spring bloom

449　in the Oyashio area adhered to Sverdrup's (1953) *CD* hypothesis, an observation consistent with

450　the conclusions of Okamoto et al (2010) and Shiozaki et al. (2014).

451　　　　　On the basis of the spring bloom onset mechanisms identified above, we classified our

452　data/images pixel by pixel based on *MLD* and *CD* differences, *MLD* deepening/shoaling, and

453　percentage of phytoplankton growth to identify spatial patterns in the mechanisms responsible for

454　the onset of the spring bloom in the NWPO (Fig. 8b). The classic *CD* hypothesis applied in the

455　area roughly north of 40ºN, including the Oyashio area. The onset of the spring bloom within the

456　band between 31ºN and 40ºN was likely associated with the cessation of winter mixed layer

457   deepening. In the area south of about 31ºN, the onset of the bloom was likely hidden by steady

458   increase of *Chl-a* due several factors discussed below.

459   **4. Discussion**

460   *4.1. The spatial extents of light- and nutrient-limited areas*

461   Using in situ observations, Limsakul et al. (2002), Liu et al. (2004), and Fujiki et al. (2014)

462   among others, have previously hypothesized that nutrients are limiting to phytoplankton growth in

463   the STA and that light is limiting in the SAA, especially during the winter. The present work has

464   shown that the spatial extents of the light- and nutrient-limited areas and the transition area

465   between them change seasonally.

466   The southernmost limit of the light-limited area occurred in the winter around 30ºN (Fig. 4e,

467   5e). Phytoplankton south of 30ºN were therefore limited by nutrients all year-round, because the

468   *MLD* was always shallower than the *CD*, even during active vertical mixing in the winter (Fig. 2p,

469   6a–c; see also Obata and Ishizaka, 1996). Phenomena seemingly inconsistent with nutrient

470   limitation were, however, apparent in the negative correlations between *Chl-a* and *SSN* (south of

471   about 35ºN) during the summer and fall (Fig. 5k-l), when nutrient-limited conditions should have

472   been more severe compared to other seasons (Fig. 5i-j).

473   The transition from positive to negative correlations between *Chl-a* and *SSN* at latitudes

27

474   around 35ºN was attributable to Eq. (1), which caused the correlation to shift from positive to

475   negative when the *SST* exceeded 23ºC, and the fact that Eq. (1) seems to be less accurate in the

476   limit of low *SSN*. The largest *SSN* estimation errors occurred at station S1 (Table 2), where at *SST*

477   > 23ºC, the top layer of in situ nitracline was about 80 m, whereas the top layer of thermocline was

478   only 20 m (Fig. 9a). The shallowest *MLD* with smallest variability (mean: 18 m, range: 11 ~ 26 m)

479   might easily entrain cold- and high *Chl-a* water from deeper layer, but hardly entrain nitrate-rich

480   deep water, the fact being the reason for the change from negative to positive correlations between

481   *SST* and *SSN* in the area with *SST* > 23ºC, and for lack of positive correlations between *Chl-a* and

482   *SSN* south of 35ºN (Fig. 5k). Same explanation also applied for the lack of *Chl-a* and *SSN* positive

483   correlation during the fall considering the facts that nitracline (~95 m) was much deeper than the

484   *MLD* (~44 m, range: 34 ~ 55 m), top layers of deep *Chl-a* maximum (~40 m) and thermocline (~52

485   m) (Fig. 9b). Severely limited nitrate flux during the summer and fall led to a condition of *SSN*

486   deficiency, as the N:P stoichiometry ratios were about 1 and 13 in the surface layer and 200 m

487   depth, respectively (see nitrate and phosphate profiles in Fig. 9). Moore et al. (2013) have also

488   shown shortage of *SSN* south of 35ºN in the NWPO.

489   Negative *Chl-a* and *MLD* correlation (Fig. 5s) also indicated that vertical mixing no longer

490   controlled *Chl-a* via *SSN* variation. Instead, it might reflect a short-term response to dilution, i.e.;

491   entrainment and recoupling of phytoplankton and zooplankton from below might lead to an

492 increase of grazing pressure (Behrenfeld, 2010). Lack of data prevented us from testing this

493 hypothesis, but the fact that zooplankton biomass contributed more than phytoplankton to total

494 biomass at 30ºN (Yamaguchi et al., 2004) might indicate that deepening of the *MLD* would entrain

495 more zooplankton than phytoplankton, and the resultant increase of grazing pressure would cause

496 the *Chl-a* to decrease.

497   It has been widely reported that light is an important factor determining phytoplankton

498 variability in the Oyashio area during the period from winter (e.g., Chiba et al., 2004) to the end

499 of the spring bloom (e.g., Saito et al., 2002; Liu et al., 2004). Our results have extended this current

500 understanding. We infer from the negative correlations between *Chl-a* and *WS* (hence *MLD*) and

501 the positive correlations between *Chl-a* and *PAR* during the summer and fall (Fig. 5g-h, 5o-p, 5s-

502 t) that light, among other factors (micronutrients, grazing), was likely an important contributor to

503 the regulation of phytoplankton biomass during the summer and fall. This result is understandable,

504 because macronutrients in the Oyashio area are still abundant, even during the summer (e.g., Saito

505 et al., 2002). It is important to note that year-round light limitation likely characterizes not only

506 the Oyashio area but also the area west of the K2–S1 section and east of the Japan/Kuril Islands

507 (Fig. 5e-f, 5r-t).

508   During the winter, a narrow band extending from about 140ºE, 35ºN southeastward was

509 characterized by a remarkable negative correlation between *Chl-a* and *SST*, and a positive

510   correlation between *Chl-a* and *SSN* was also clearly apparent in the same area. These correlations

511   were especially apparent with respect to variable anomalies (Fig. 5a, 5i) but were not accompanied

512   by positive correlations between *Chl-a* and *MLD*. These patterns reflect the fact that both seasonal

513   and interannual *Chl-a* variations in this narrow band were not simply associated with nutrient

514   variability driven by conventional vertical mixing, but were more associated with physical factors,

515   including, inter alia, mesoscale eddies, Kuroshio meanders, front variability, and upwelling events

516   (e.g., Sasai et al., 2010).

517   *4.2. Relevance of bloom onset mechanisms and discrepancies with previously reported*

518   *mechanisms*

519   Obata and Ishizaka (1996) analyzed data from around the globe and were among the pioneers

520   who verified that Sverdrup's (1953) *CD* hypothesis could be broadly applied to explain the onset

521   of the spring bloom in the NWPO. They mentioned, however, that at latitudes south of 30ºN, the

522   *MLD* was shallower than the *CD* throughout the year, a conclusion consistent with our results (Fig.

523   6). Therefore, at least in the area south of 30ºN, the onset of the spring bloom should not follow

524   the *CD* model, because phytoplankton biomass is limited by nutrients rather than light, even during

525   the winter (see Fig. 5e, 6a–c). This pattern of limitation has also been observed in the subtropical

526   North Atlantic (e.g., Dutkiewicz et al., 2001; Follows and Dutkiewicz, 2001).

527   Obata and Ishizaka (1996) did not discuss the mechanism responsible for the onset of the

528   bloom south of 30ºN, because they considered spring blooms to be uncommon there. Based on the

529   analysis of Chiswell (2011), we think that there is spring bloom south of 30ºN, but it is initiated

530   when the *MLD* is shallower than the *CD*, and phytoplankton growth is positive during the winter.

531   In addition, we think that the onset of the spring bloom in this area (roughly south of about 31ºN,

532   Fig. 8b) was likely hidden by the increase of *Chl-a* that begins in the fall. The initial increase of

533   *Chl-a* in early fall (October) might be attributable to entrainment of deep *Chl-a* maximum, rather

534   than of nutrients, because top layer of nitricline (~95 m) was much deeper than that of deep *Chl-a*

535   maximum (~44 m) (Fig. 9b). Further mixed layer deepening led to entrainments of both nutrient

536   and deep *Chl-a* maximum, thereby caused remarkable increase of *Chl-a* in mid fall. Mixed layer

537   deepening possibly also led to increase *Chl-a* via dilution effects that decouple phytoplankton and

538   zooplankton during deepening of the *MLD* (Behrenfeld, 2010). This area also roughly overlies the

539   area characterized by a phytoplankton bloom that peaks in late winter (Fig. 8a).

540   Our classification of spring bloom onset mechanisms in the area between 31ºN and 40ºN (Fig.

541   8b) is in general consistent with the results of Shiozaki et al. (2014), especially south of 35°N,

542   where the onset of the spring bloom was not associated with shoaling of the *MLD*. Shiozaki et al.

543   (2014) have suggested that the timing of the onset of the bloom in the area north of 35°N (but

544   south of 40°N) is associated with complex factors, including lateral advection of high *Chl-a*

545 concentrations. It is clear from Fig. 8a in Shiozaki et al. (2014), however, that the onset of the

546 bloom took place only at the time when winter deepening of the *MLD* stopped or thereafter. We

547 therefore characterized this area by a single bloom onset mechanism, which was associated with a

548 cessation of mixed layer deepening or a subsequent shoaling of the MLD. This mechanism largely

549 encompasses the 'stratitification-onset' (Chiswell, 2011), and 'turbulence weakening/shutdown'

550 (Taylor and Ferrari, 2011; Shiozaki et al., 2014) mechanisms. This area also coincides with the

551 area where the peak of the spring bloom occurred around April (Fig. 8a).

552   The fact that the onset of the spring bloom adhered to the *CD* hypothesis in much of the area

553 north of 40°N and in the Oyashio area (Fig. 8a) was consistent with the observations of Obata and

554 Ishizaka (1996) and Okamoto et al. (2010) in the former case and with the observations of Shiozaki

555 et al. (2014) in the latter case. A mixed classification, however, emerged in the area between 150°E

556 and 160°E and between 40°N and 45°N which is referred to as transition region mode water by

557 Shiozaki et al. (2014). This mixed classification area reflects the large spatial variability of the

558 mechanism responsible for the onset of the spring bloom. However, because the time of the onset

559 of the bloom in this mixed classification area took place only after the cessation of mixed layer

560 deepening (or 'turbulence weakening' in the terminology of Shiozaki et al., 2014), much of this

561 area was classified in the same way as most of the area between 31°N and 40°N, which was also

562 characterized by a peak of the spring bloom in May or June (Fig. 8a).

563   The data we used provided a temporal resolution of one month and could only resolve the

564   time of the onset of the spring bloom to within one month. The result was that bloom onset

565   mechanisms were categorized in only three ways: first, the onset of the bloom was consistent with

566   Sverdrup's *CD* model (north of 40°N); second, the onset of the bloom was associated with

567   cessation of mixed layer deepening (31°N~40°N); and third, the onset of the bloom was likely

568   hidden by a steady increase of *Chl-a* during *MLD* deepening (south of 31°N). Our monthly data

569   could not be used to resolve the second category of bloom onset mechanism into more detailed

570   processes such as 'stratification-onset' or 'turbulence weakening/shutdown' because the difference

571   in the timing of those processes is definitely less than one month. Because our classification is

572   based on average monthly data, the spatial extents of the classified areas are by no means constant.

573   Global warming and large-scale climatic changes might cause the areas of bloom onset

574   mechanisms to shift interchangeably across borders. For instance; the second and third categories

575   would be expected to shift northward if the *MLD* shoals in conjunction with global warming and

576   weakening of the Aleutian Low pressure system.

577   **5. Conclusions**

578   A summary of our results regarding the factors that determine *Chl-a* variations is as follows:

579   (1) the areas characterized by light-limited and nutrient-limited conditions as well as the

33

580 intermediate transitional areas changed seasonally; (2) during the winter, light and nutrients

581 obviously limited phytoplankton biomass north of 30°N and south of 30°N, respectively; (3)

582 during the spring and fall, light limitation of phytoplankton biomass was more restricted and

583 characterized the areas east of the Japan/Kuril Islands and/or north of 40°N. Nutrient limitation

584 was likewise more confined and characterized the areas south of 35°N; and (4) during the summer,

585 nutrients mainly limited phytoplankton biomass, except in the areas east of the Japan/Kuril Islands

586 and north of 45°N.

587   We categorized the mechanisms responsible for the onset of the spring bloom into three main

588 groups. The first was mainly confined to the area south of around 31°N and was associated with a

589 bloom onset that probably occurred within the period of steady increase of *Chl-a* that accompanied

590 deepening of the *MLD* during the fall. The second was confined mainly to the area between 31°N

591 and 40°N and was associated a cessation of mixed layer deepening. The third mechanism

592 corresponded to the classic *CD* hypothesis and was largely confined to the area north of 40°N,

593 including the Oyashio area.

34

597   data. We also acknowledge the Remote Sensing Systems and Physical Oceanography-Distributed

598   Active Archive Center (PO.DAAC), Jet Propulsion Laboratory, for processing and distributing sea

599   surface temperature and microwave-sensor-retrieved satellite data, respectively.

600   **References**

601   Alvera-Azcarate, A., Barth, A., Beckers, J.-M., & Weisberg, R.H. (2007). Multivariate

602   reconstruction of missing data in sea surface temperature, chlorophyll, and wind fields.

603   *Journal of Geophysical Research, 112*, C03008, doi:10.1029/2006JC003660.

604   Bailey, S.W. & Werdell, P.J. (2006). A multi-sensor approach for the on-orbit validation of ocean

605   color satellite data products. *Remote Sensing of Environment, 102*, 12 – 23.

606   Behrenfeld, M.J. (2010). Abandoning Sverdrup's Critical Depth Hypothesis on phytoplankton

607   blooms. *Ecology, 91(4),* 977–989.

608   Behrenfeld, M.J., & Falkowski, P.G. (1997). Photosynthetic rates derived from satellite-based

609   chlorophyll concentration. *Limnology and Oceanography, 42*, 1–20.

610   Chiba, S., Ono, T., Tadokoro, K., Midorikawa, T., & Saino, T. (2004). Increased stratification and

611   decreased lower trophic level productivity in the Oyashio region of the North Pacific: A 30-

612   year retrospective study. *Journal of Oceanography, 60*, 149–162.

613   Chiswell, S.M. (2011). Annual cycles and spring blooms in phytoplankton: don't abandon

614   Sverdrup completely. *Marine Ecology Progress Series, 443*, 39–50.

615   Cohen, J., Barlow, M., & Saito, K. (2009). Decadal fluctuations in planetary wave forcing

616   modulate global warming in late boreal winter. *Journal of Climate, 22*, 4418–4426.

617   Dutkiewicz, S., Follows, M., Marshall, J., Gregg, W.W. (2001). Interannual variability of the

618   phytoplankton abundances in the North Atlantic. *Deep-Sea Research II, 48*, 2323 – 2344.

619   Eppley, R.W. (1972). Temperature and phytoplankton growth in the sea. *Fishery Bulletin, 70(4)*,

620   1063–1085.

621   Follows, M., & Dutkiewicz, S. (2001). Meteorological modulation of the North Atlantic spring

622   bloom. *Deep-Sea Research II, 49*, 321 – 344.

623   Freeland, H., Denman, K., Wong, C.S., Whitney, F., & Jacques, R. (1997). Evidence of change in

624   the winter mixed layer in the Northeast Pacific Ocean. *Deep-Sea Research I, 44*, 2117–2129.

625   Froiun, R. & Pinker, R.T. (1995). Estimating photosynthetically active radiation (PAR) at the

626   earth's surface from satellite observations. *Remote Sensing of Environment, 51(1)*, 98–107.

627   Frouin, R. & McPherson, J. (2012). Estimating photosynthetically available radiation at the ocean

628   surface from GOCI data. *Ocean Science Journal, 47(3)*, 313–321.

629   Fujiki, T., Matsumoto, K., Mino, Y., Sasaoka, K., Wakita, M., Kawakami, H., Honda, M.C.,

630   Watanabe, S., & Saino, T. (2014). Seasonal cycle of phytoplankton community structure and

631   photo-physiological state in the western subarctic gyre of the North Pacific. *Limnology and*

632   *Oceanography, 59(3),* 887–900.

633   Goes, J.I., Saino, T., Oaku, H., Ishizaka, J., Wong, C.S., & Nojiri, Y. (2000). Basin scale estimates

634   of sea surface nitrate and new production from remotely sensed sea surface temperature and

635   chlorophyll. *Geophysical Research Letters*, *27(9)*, 1263–1266.

636   Goes, J.I., Sasaoka, K., Gomes, H.D.R., Saitoh, S., & Saino, T. (2004). A comparison of the

637   seasonality and interannual variability of phytoplankton biomass and production in the

638   western and eastern gyres of the subarctic Pacific using multi-sensor satellite data. *Journal of*

639   *Oceanography, 60,* 75–91.

640   Hanawa, K., & Mitsudera, H. (1987). Variation of water system distribution in the Sanriku Coastal

641   Area. *Journal of the Oceanographical Society of Japan, 42*, 435–446.

642   Holm-Hansen, O., & Riemann, B. (1978). Chlorophyll a determination: improvements in

643   methodology. *Oikos, 30*, 438–447.

644   Limsakul A. Saino, T., Goes, J.I., & Midorikawa, T. (2002). Seasonal variability in the lower

645   trophic level environments of the western subtropical Pacific and Oyashio Waters – a

646   retrospective study. *Deep-Sea Research, II 49*, 5487–5512.

647   Liu, H., Suzuki, K., & Saito, H. (2004). Community structure and dynamics of phytoplankton in

648   the western subarctic Pacific Ocean: A synthesis. *Journal of Oceanography, 60*, 119 – 137.

649   Monterey, G. & Levitus, S. (1997). Seasonal variability of mixed layer depth for the world ocean.

650   *NOAA Atlas NESDIS 14*, 100 pp.

651   Moore, C.M., Mills, M.M., Arrigo, K.R., Berman-Frank, I., Bopp, L., Boyd, P.W., Galbralth, E.D.,

652   Gelder, R.J., Guleu, C., Jaccard, S.L., Jickells, T.D., La Roche, J., Lenton, T.M., Mahowald,

653   N.M., Maranon, E., Marinov, I., Moore, J.K., Nakatsuka, T., Oschlies, A., Saito, M.A.,

654   Thingstad, T.F., Tsuda, A., & Ulloa, O. (2013). Processes and patterns of oceanic nutrient

655   limitation. *Nature Geoscience, 6*, 701 − 710.

656   Morel, A., Huot, Y., Gentili, B., Werdell, P.J., Hooker, S.B., & Franz, B.A. (2007). Examining the

657   consistency of products derived from various ocean color sensors in open ocean (Case 1)

658   waters in the perspective of a multi-sensor approach. *Remote Sensing of Environment, 111*,

659   69–88.

660   Obata, A. & Ishizaka, J. (1996). Global verification of critical depth theory for phytoplankton

661   bloom with climatological in situ temperature and satellite ocean color data. *Journal of*

662   *Geophysical Research, 101(C9)*, 20,657 − 20,667.

663   Okamoto, S., Hirawake, T., & Saitoh, S. (2010). Interannual variability in the magnitude and

664   timing of the spring bloom in the Oyashio region. *Deep-Sea Research II, 57*, 1608–1617.

665   O'Reilly, J.E., Maritorena, S., Mitchell, B.G., Siegel, D.A., Carder, K.L., Garver, S.A., Kahru, M.,

666   & McClain, C.R. (1998). Ocean color chlorophyll algorithms for SeaWiFS. *Journal of*

667   *Geophysical Research*, *103*, 24937–24953.

668   Parsons, T.R., Takahashi, M., & Hargrave, B. (1984). Biological oceanographic processes. *3ʳᵈ*

669   *Edition, Pergamon Press, Oxford & New York*, 344 pp.

670   Saito, H., Tsuda, A., & Kasai, H. (2002). Nutrient and plankton dynamics in the Oyashio region of

671   the western subarctic Pacific Ocean. *Deep Sea Research II, 49(24-25)*, 5463 – 5486.

672   Sasai, Y., Richards, K.J., Ishida, A., & Sasaki, H. (2010). Effects of cyclonic mesoscale eddies on

673   the marine ecosystem on the Kuroshio Extension region using an eddy-resolving coupled

674   physical-biological model. *Ocean Dynamics, 60*, 693 – 704.

675   Sasaoka, K., Saitoh, S., Asanuma, I., Imai, K., Honda, M., Nojiri, Y., & Saino, T. (2002). Temporal

676   and spatial variability of chlorophyll-a in the western subarctic Pacific determined from

677   satellite and ship observations from 1997 to 1999. *Deep-Sea Research II*, *49*, 5557–5576.

678   Shiozaki, T., Ito, S.I., Takahashi, K., Saito, H., Nagata, T., & Furuya, K. (2014). Regional

679   variability of factors controlling the onset timing and magnitude of spring algal blooms in the

680   northwestern North Pacific. *Journal Geophysical Research, 119*, 253–265.

681   Siegel, D.A., Doney, S.C., & Yoder, J.A. (2002). The North Atlantic spring phytoplankton bloom

682   and Sverdrup's critical depth hypothesis. *Science, 296*, 730–733.

683   Siswanto, E., Tang, J., Yamaguchi, H., Ahn, Y.H., Ishizaka, J., Yoo, S., Kim, S.W., Kiyomoto, Y.,

684   Yamada, K., Chiang, C., & Kawamura, H. (2011). Empirical ocean-color algorithms to

685   retrieve chlorophyll-a, total suspended matter, and colored dissolved organic matter

686   absorption coefficient in the Yellow and East China Seas. *Journal of Oceanography, 67(5)*,

687   627 – 650.

688 Sverdrup, H. U. (1953). On conditions for the vernal blooming of phytoplankton. *J. du Conseil*

689   *International pour l'Exploration de la Mer, 18*, 287–295.

690 Taylor, J.R., & Ferrari, R. (2011). Shutdown of turbulent convection as a new criterion for the

691   onset of spring phytoplankton blooms. *Limnology and Oceanography, 566(6)*, 2293 – 2307.

692 Thomas, A.C., Strub, P.T., Weatherbee, R.A., & James, C. (2012). Satellite views of Pacific

693   chlorophyll variability: Comparison to physical variability, local versus nonlocal influences

694   and links to climate indices. *Deep-Sea Research II, 77-80*, 99 – 116.

695 Vantrepotte, V. & Me'lin, F. (2009). Temporal variability of 10-year global SeaWiFS time-series

696   of phytoplankton chlorophyll a concentration. *ICES Journal of Marine Science, 66,* 1547 –

697   1556.

698 Wang, L., Chen, W., & Huang, R. (2008). Interdecadal modulation of PDO on the impact of ENSO

699   on the east Asian winter monsoon. *Geophysical Research Letters, 35*, L20702,

700   doi:10.1029/2008GL035287.

701 Whitney, F.A., & Freeland, H.J. (1999). Variability in upper-ocean water properties in the NE

702   Pacific Ocean. *Deep-Sea Research II, 46*, 2351–2370.

703 Yamaguchi, A., Watanabe, Y., Ishida, H., Harimoto, T., Furusawa, K., Suzuki, S., Ishizaka, J.,

704   Ikeda, T., & Takahashi, M.C. (2004). Latitudinal differences in the planktonic biomass and

705   community structure down to the greater depths in the western north Pacific. *Journal of*

706   *Oceanography, 60*, 773 – 787.

707   Yasuda, I. (2003). Hydrographic structure and variability in the Kuroshio-Oyashio transition

708   area. *Journal of Oceanography, 59*, 389 – 402.

709   Yoder, J.A., & Kennelly, M.A. (2003). Seasonal and ENSO variability in global ocean

710   phytoplankton chlorophyll derived from 4 years of SeaWiFS measurements. *Global*

711   *Biogeochemical Cycles, 17(4)*, 1112.

712   Yoshie, N., Yamanaka, Y., Kishi, M.J., & Saito, H. (2003). One dimensional ecosystem model

713   simulation of the effects of vertical dilution by the winter mixing on the spring diatom bloom

714   *Journal of Oceanography,* 59, 563–571.

715   Yoo, S., Batchelder, H.P., Peterson, W.T., & Sydeman, W.J. (2008). Seasonal, interannual and

716   event scale variation in the North Pacific ecosystems. *Progress in Oceanography*, *77*, 155–

717   181.

Figure Captions

719 **Fig. 1.** (a) Map of the study region, the NWPO, which covers the SAA and the STA, where

720 biogeochemical time-series stations K2 and S1, respectively, are located. The green dashed circle

721 denotes approximately the location of the Oyashio area. The red dashed line is the K2–S1 line. (b)

722 Meridional variations along the K2-S1 line of correlations that resulted from regressions between

723 variables retrieved by two different sensors/sources. Green, black, cyan, blue, and red lines

724 correspond to SeaWiFS vs. MODIS *Chl-a*, AVHRR vs. MODIS *SST*, CCMP vs. WindSat *WS*,

725 GODAS vs. Argo float *MLD*, and SeaWiFS vs. MODIS *PAR*, respectively. All correlations are

726 statistically significant at $p < 0.05$. Horizontal dashed lines indicate the latitudes of stations K2 and

727 S1.

728

729 **Fig. 2.** Monthly means of all satellite-based and reanalyzed variables derived from the 16-year

730 dataset (September 1997 to June 2013) at eight latitudes along the K2-S1 line. Left column (a–h)

731 shows the seasonal cycles for *WS* (cyan), *PAR* (red), *SST* (black), and *SSN* (yellow). Right column

732 (i–p) shows the seasonal cycles for *Chl-a* (light green), *r* (dashed dark green), *MLD* (blue), and

733 *CD* (gray). Yellow and red dots in (a) and (h) are in situ data of *SSN* and *PAR*, respectively. Green,

734 blue, and gray dots in (i) and (p) are in situ data of *Chl-a*, *MLD*, and *CD*, respectively.

735

736 **Fig. 3.** Spatial variation of significant ($p < 0.05$) correlation coefficients between *Chl-a* and *WS*

737 (a), *MLD* (b), *SSN* (c), *SST* (d), and *PAR* (e) based on 16-year monthly datasets (N = 190). The

738 areas with insignificant correlation coefficients ($p > 0.05$) are masked (white areas). Stations K2

739 and S1 (circles) and the section between them (dashed line) are shown on all maps.

740

741 **Fig. 4.** Spatial variations of significant ($p < 0.05$) correlations between *Chl-a* and *SST* during winter

742 (a), spring (b), summer (c), and fall (d). Panels (e–h), (i–l), (m–p), and (q–t) are the same as panels

743 (a–h), except that the correlations are between *Chl-a* and *PAR*, between *Chl-a* and *SSN*, between

744 *Chl-a* and *WS*, and between *Chl-a* and *MLD*, respectively. White areas, circles, and dashed lines

745 have the same meaning as in Fig. 3.

746

747 **Fig. 5.** Same as Fig. 4, except that the correlation coefficients were derived by using anomalies of

748 variables (after removing seasonal means and trends from the time-series).

749

750 **Fig. 6.** Spatial variations of the monthly means of the differences between the *MLD* and *CD* (m).

751 White contours indicate where the difference is 0 (*MLD = CD*). Black dashed circle in (c) indicates

752 the approximate location of the Oyashio area. Stations K2 and S1 (circles) and their section (dashed

753 line) are shown in all panels.

754

755 **Fig. 7.** Spatial variations of the monthly mean rates of change of *Chl-a* (*r*, % per month). White

756 contour indicates $r = 0$. The black dashed circle in (d) indicates the approximate location of the

757 Oyashio area. Stations K2 and S1 (circles) and their section (dashed line) are shown in all panels.

758

759 **Fig. 8.** (a) Meridional variation of the month when the spring bloom peaks. (b) Meridional

760 classification of spring bloom onset mechanisms. Blue, red, and green areas denote bloom onsets

761 associated with fall deepening of the *MLD*, cessation of winter mixed layer deepening, and the

762 Sverdrup (1953) *CD* hypothesis, respectively. Stations K2 and S1 (circles) and their section

763 (dashed line) are shown in all panels. White areas, mainly north of 40ºN, denote pixels where the

764 bloom onset could not be classified based on our bloom onset mechanism classification. Dashed

765 black circle in (a) or (b) indicates the approximate location of the Oyashio area.

766

767 **Fig. 9**. Vertical profiles of in situ *Chl-a* (green), nitrate (red), phosphate (blue), and temperature

768 (yellow) collected at the S1 in the summer (a, 20 July 2011) and fall (b, 9 November 2010) by

769 research vessel *Mirai*. Solid and dashed black lines indicate the seasonal mean and range (upper

770 and lower limits) of *MLD*s.

771

Table Captions

773 **Table 1**

774 Detailed information about the cruises (cruise names, periods) during which in situ data were

775 collected to verify satellite-retrieved and/or reanalyzed data.

776

777 **Table 2**

778 Relative percentage differences (%) between satellite/reanalyzed geophysical variables and in situ

779 measurements and absolute percentage differences (%) between satellite-derived *Chl-a* and in situ
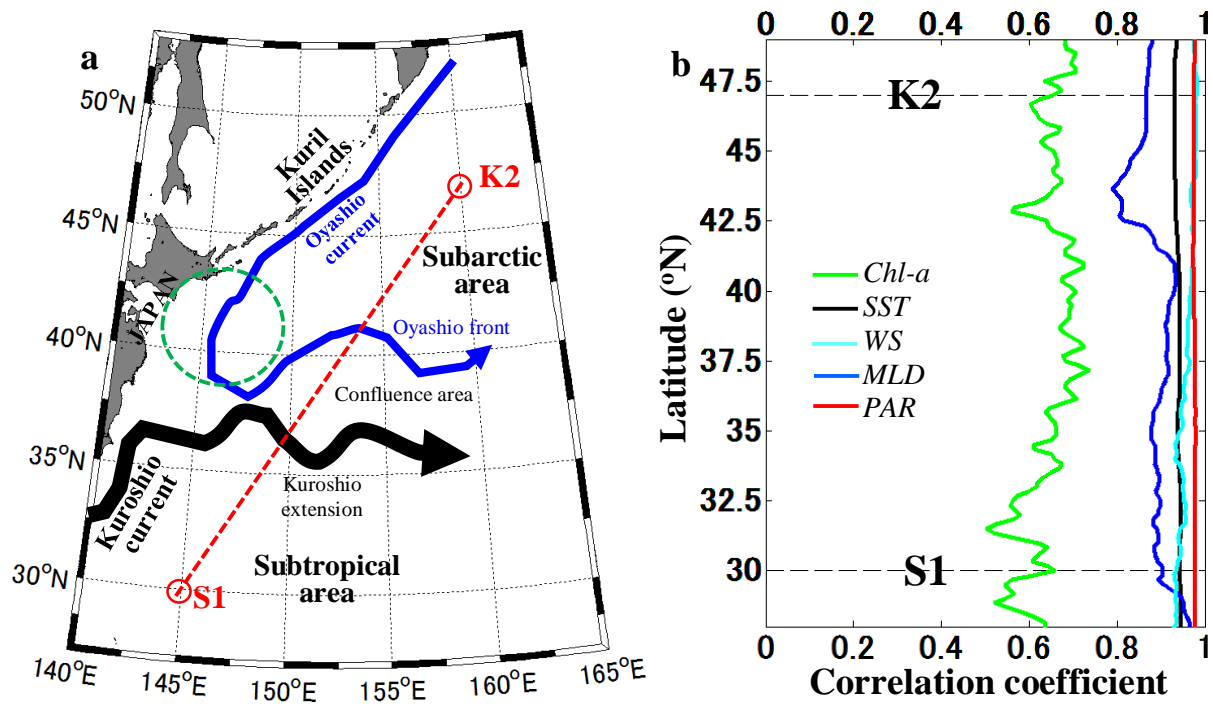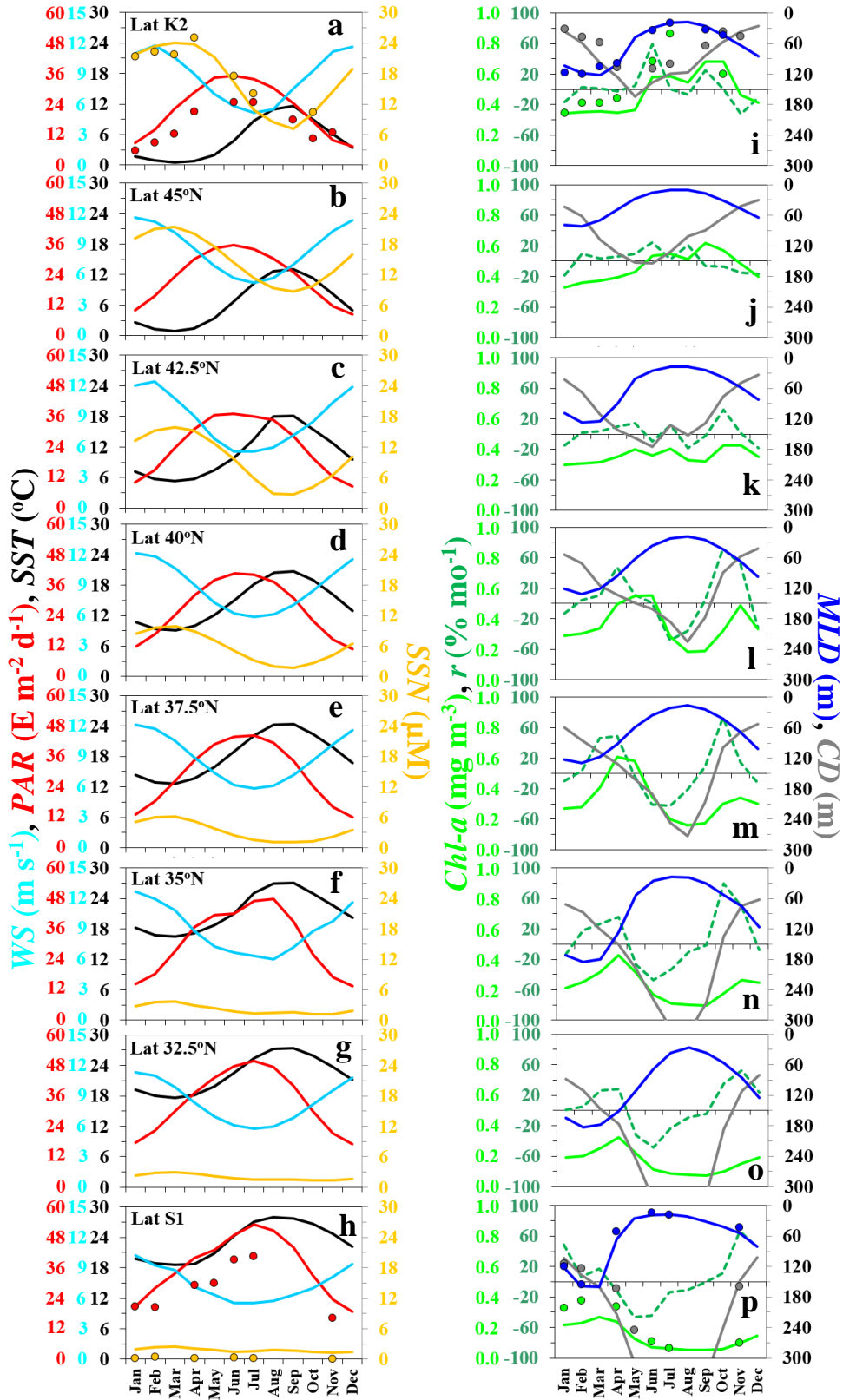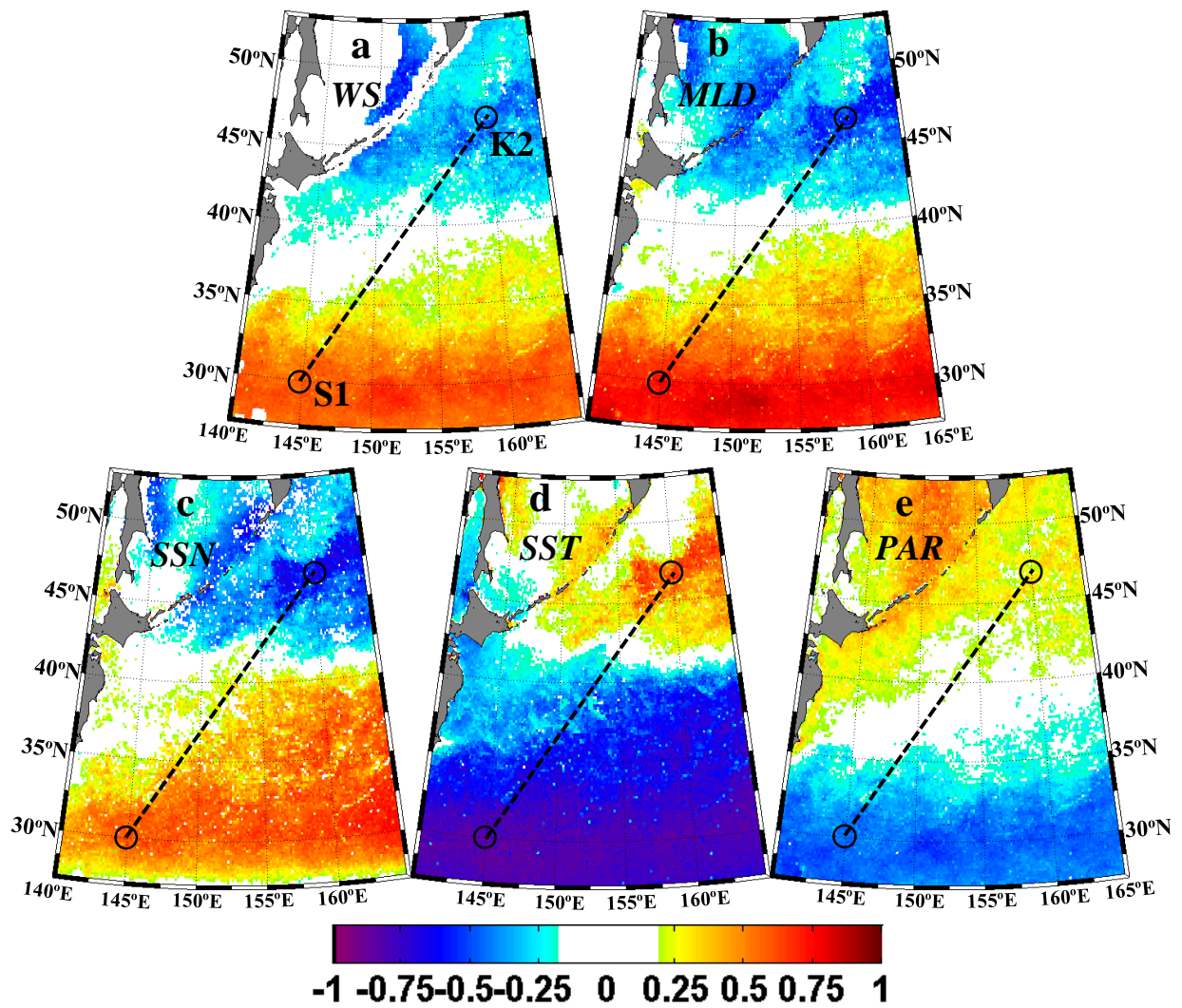
780 *Chl-a* at the K2 and S1 time-series stations.
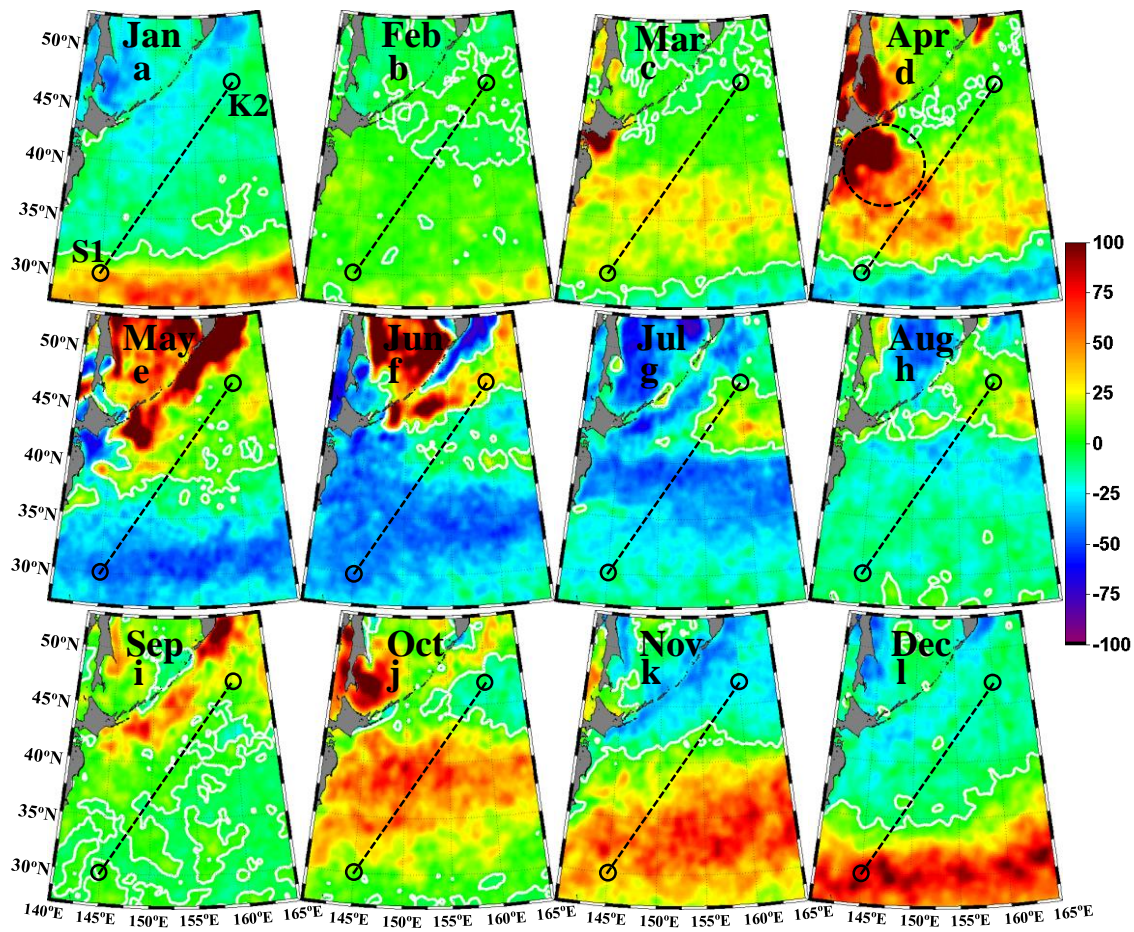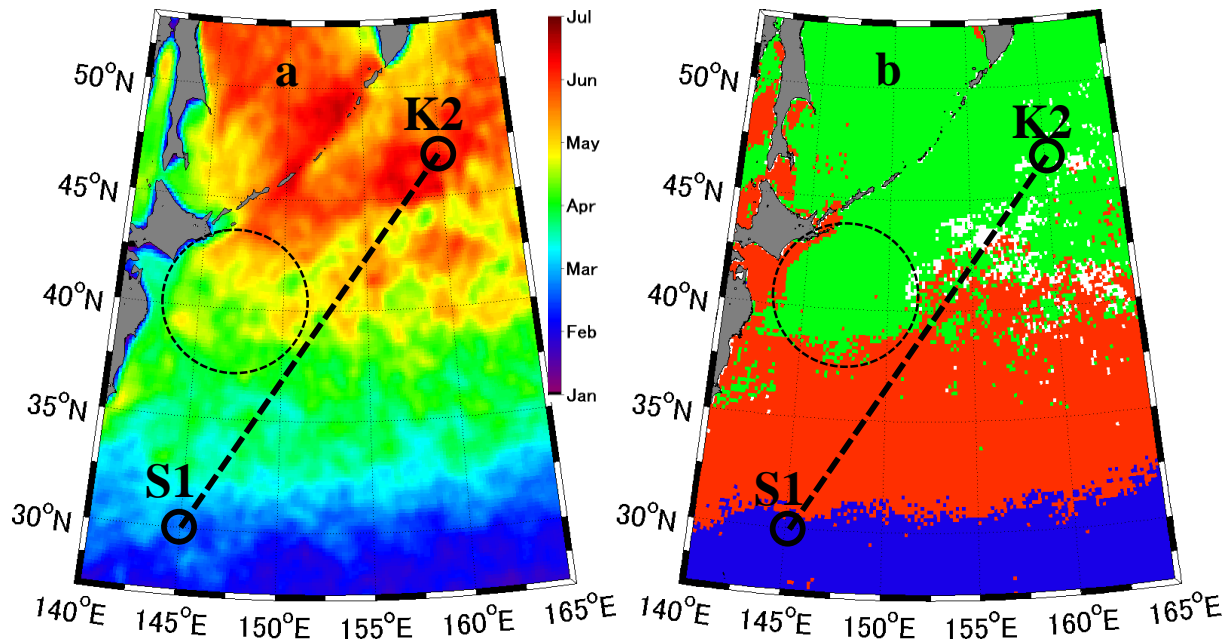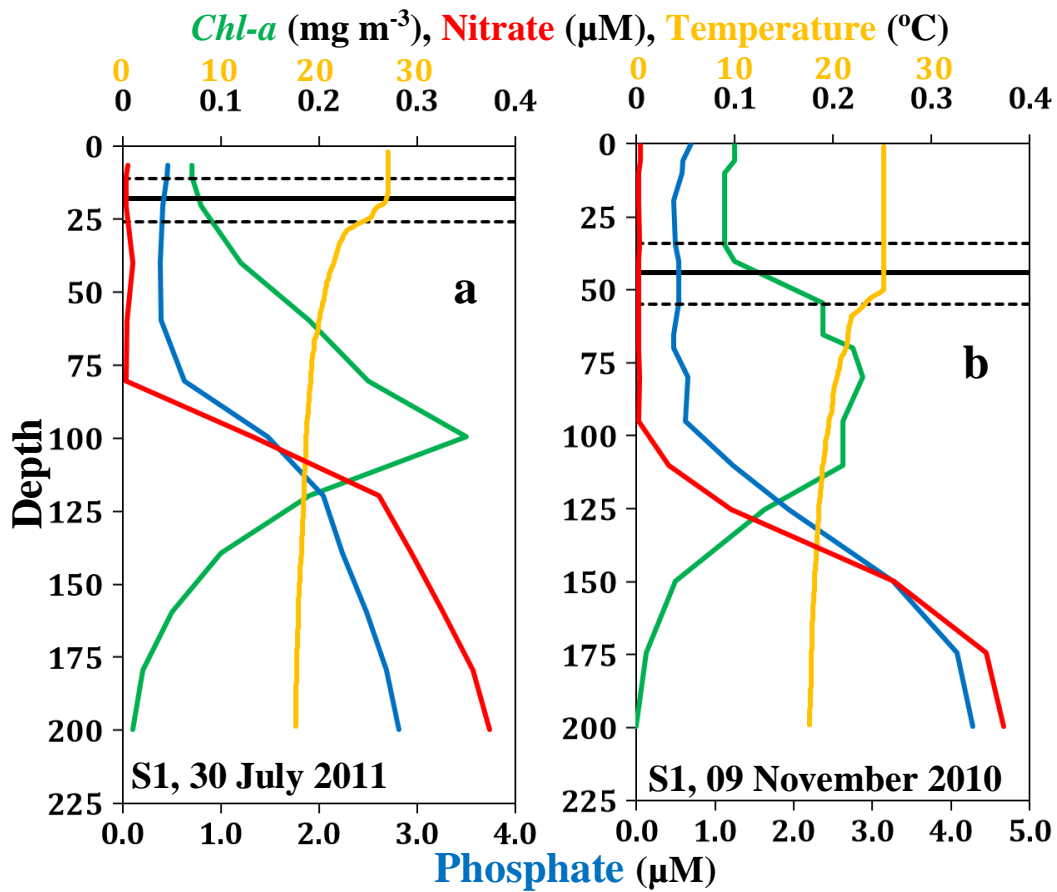
781

Figure 1.

Figure 2.

Figure 3.
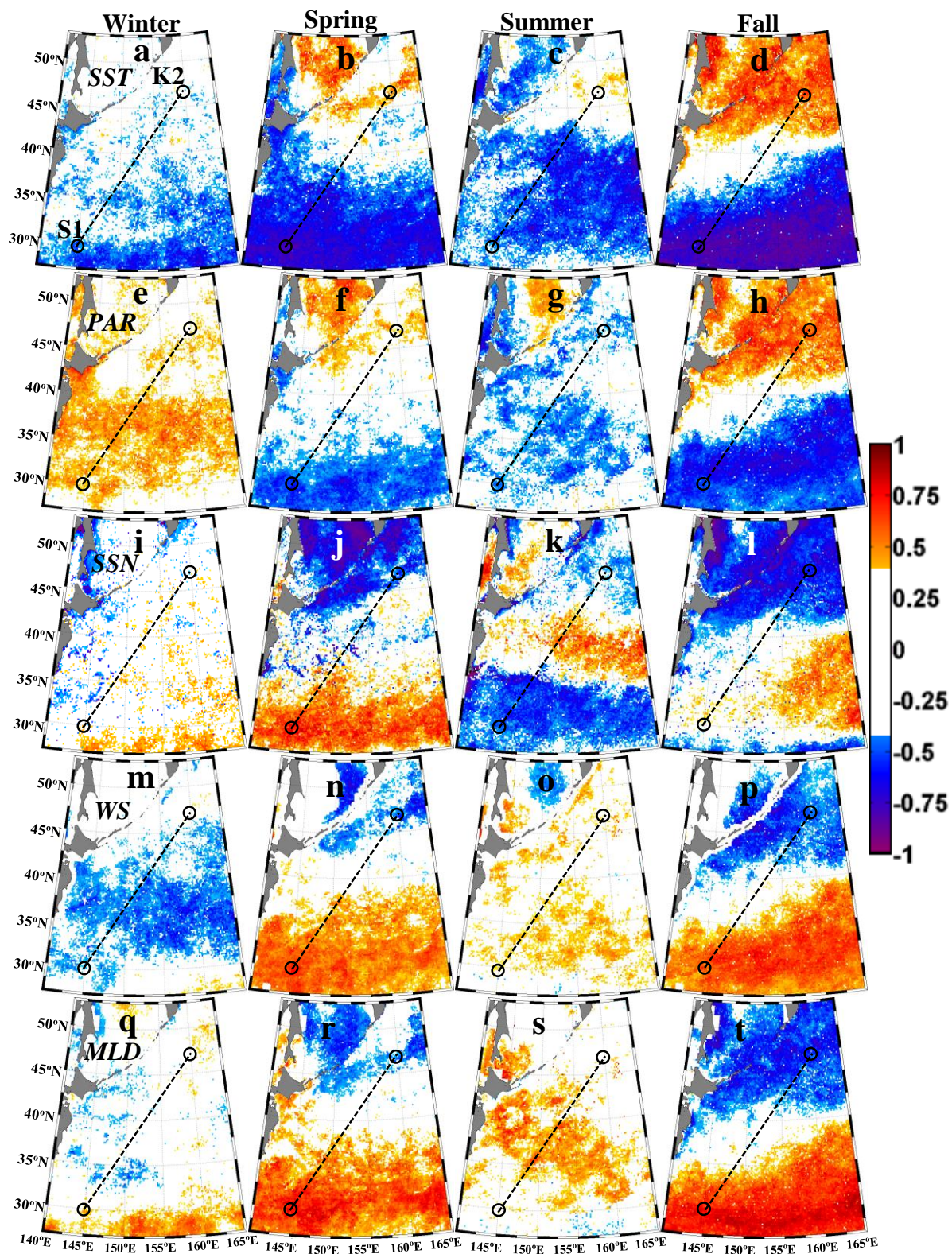
Figure 4.
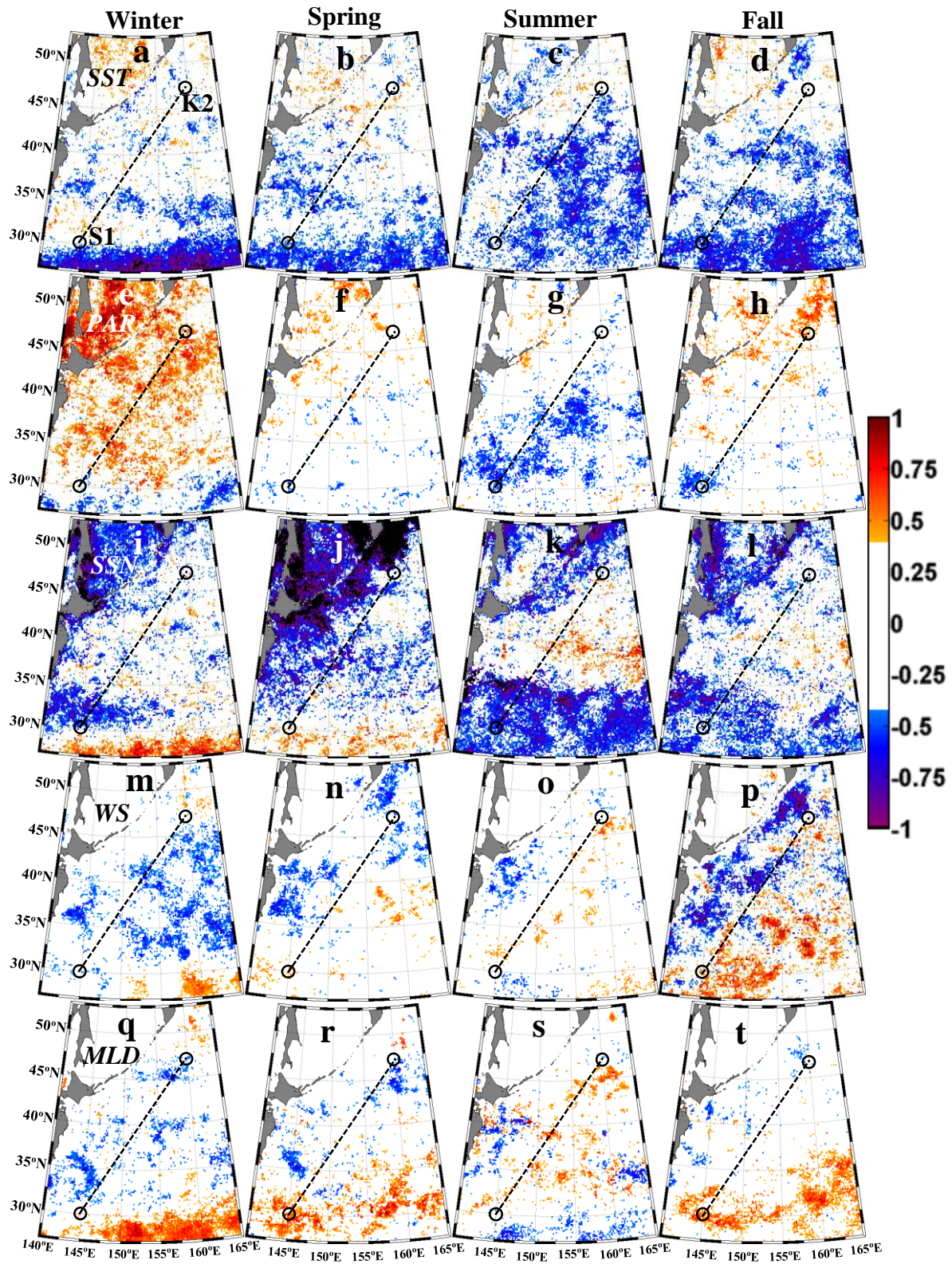
Figure 5.
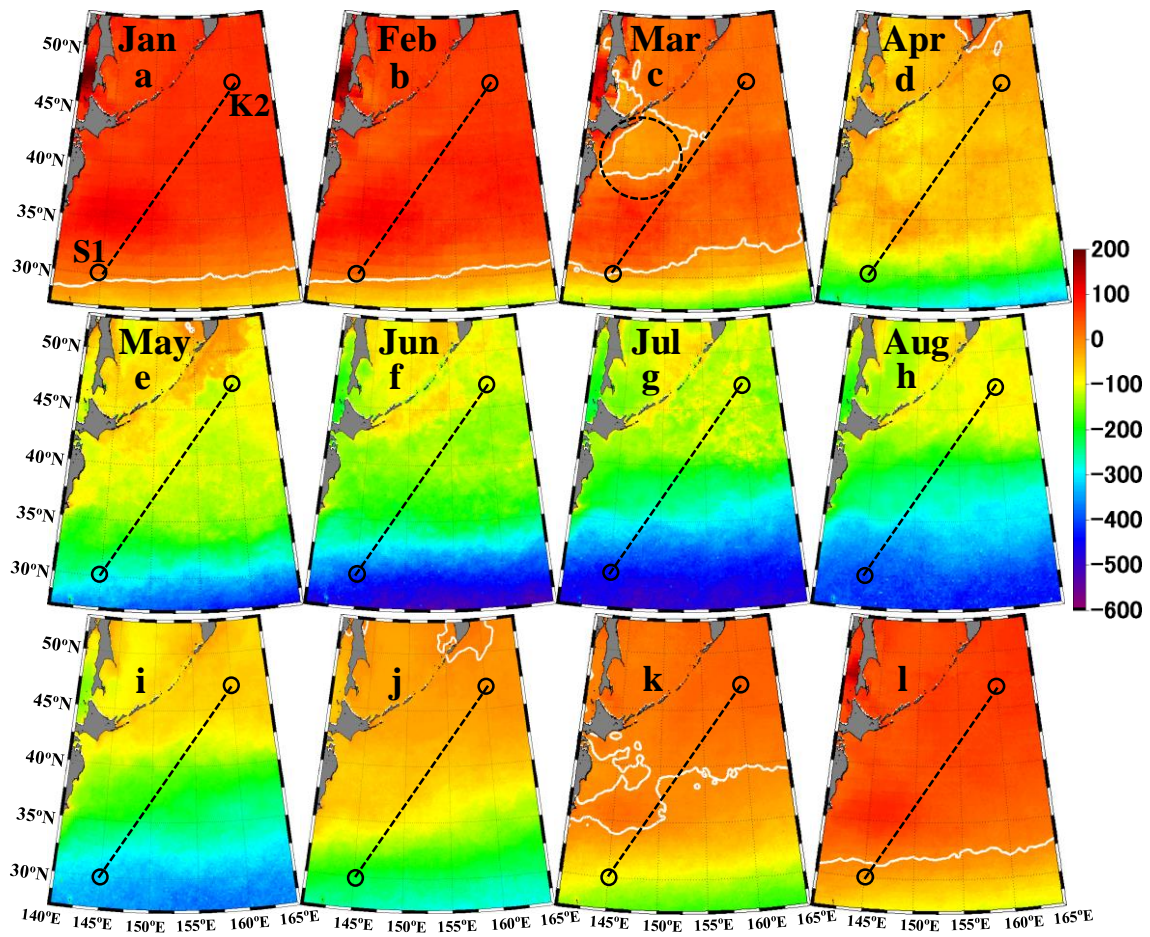
Figure 6.

Figure 7.

Figure 8.

Figure 9.